RNF169 limits 53BP1 deposition at DSBs to stimulate single-strand annealing repair

Liwei An[a,b], Chao Dong[a], Junshi Li[a], Jie Chen[a], Jingsong Yuan[c], Jun Huang[d], Kui Ming Chan[e], Cheng-han Yu[a], and Michael S. Y. Huen[a,b,f,1]

[a]School of Biomedical Sciences, Li Ka Shing (LKS) Faculty of Medicine, The University of Hong Kong, Hong Kong S.A.R.; [b]Institute of Synthetic Biology, Shenzhen Institutes of Advanced Technology, Chinese Academy of Sciences, Shenzhen 518055, P.R. China; [c]Department of Radiation Oncology, Center for Radiological Research, Columbia University Medical Center, NY 10032; [d]Life Sciences Institute and Innovation Center for Cell Signaling Network, Zhejiang University, Hangzhou, Zhejiang 310058, P.R. China; [e]Department of Biomedical Sciences, City University of Hong Kong, Hong Kong S.A.R.; and [f]State Key Laboratory of Brain and Cognitive Sciences, The University of Hong Kong, Hong Kong S.A.R.

Edited by James E. Haber, Brandeis University, Waltham, MA, and approved July 17, 2018 (received for review March 20, 2018)

Unrestrained 53BP1 activity at DNA double-strand breaks (DSBs) hampers DNA end resection and upsets DSB repair pathway choice. RNF169 acts as a molecular rheostat to limit 53BP1 deposition at DSBs, but how this fine balance translates to DSB repair control remains undefined. In striking contrast to 53BP1, ChIP analyses of A*si*SI-induced DSBs unveiled that RNF169 exhibits robust accumulation at DNA end-proximal regions and preferentially targets resected, RPA-bound DSBs. Accordingly, we found that RNF169 promotes CtIP-dependent DSB resection and favors homology-mediated DSB repair, and further showed that RNF169 dose-dependently stimulates single-strand annealing repair, in part, by alleviating the 53BP1-imposed barrier to DSB end resection. Our results highlight the interplay of RNF169 with 53BP1 in fine-tuning choice of DSB repair pathways.

RNF169 | 53BP1 | DNA double-strand breaks | DNA damage | single-strand annealing repair

DNA double-strand breaks (DSBs) pose serious threats to genome integrity and cell viability. Unrepaired DSBs not only perturb gene expression programs but can fuel chromosome translocation and chromosome missegregation (1–3), leading to permanent cell arrest, premature cell senescence, and cell death (4). To mend broken DNA in a timely manner, cells deploy multiple DSB repair pathways, namely classical nonhomologous end joining (cNHEJ), alternative nonhomologous end joining (aNHEJ), homologous recombination (HR), and single-strand annealing (SSA) (5, 6), to suppress the otherwise deleterious effects of persistent DSBs in cell proliferation and animal development.

cNHEJ represents the predominant DSB repair pathway in mammalian cells, involves no or limited DNA end processing, and does not require sequence homology (7). During cNHEJ, DNA ends are bound by the Ku70/Ku80 complex (Ku) to prevent end resection by nucleases (8). The Ku complex serves as a platform for docking additional NHEJ factors including DNA-PKcs, Artemis, DNA Ligase IV, XRCC4, XLF, and PAXX. By contrast, the aNHEJ, HR, and SSA repair pathways favor resected DSB intermediates that bear 3′ single-strand DNA (ssDNA) overhangs (9). DNA end resection entails the coordinated nucleolytic degradation of 5′ DNA strands and is executed by a cohort of nucleolytic and DNA unwinding activities (10). The mammalian MRE11-RAD50-NBS1 (MRN)/CtIP complex plays an initiating role in DNA end resection and exposes short 3′ ssDNA tails. At this stage, aNHEJ machineries can rejoin broken DSB ends by annealing two ssDNA overhangs that carry microhomologies. Key components of aNHEJ include PARP-1, DNA Ligase III, and DNA polymerase θ. Further DSB processing by EXO1, DNA2, and BLM results in extensively resected ssDNAs that prime HR and SSA repair. HR repair is activated strictly in S and G2 phases of the cell cycle when sister chromatids are available and is considered an error-free repair pathway. In an HR reaction, the RAD51 recombinase nucleates onto ssDNAs at resected DSBs to form nucleoprotein filaments that catalyze homology search and strand invasion events. SSA, however, is adapted to repair DSBs at genomic loci bearing repetitive DNA sequences. The SSA machineries appear to be evolutionarily conserved (11–13) and require extensive DNA end resection to reveal flanking homologous sequence. SSA ensues when the DNA annealing factor RAD52 coats ssDNA overhangs and mediates annealing of DNA molecules that bear homology (14). The nonhomologous 3′ ssDNA tails at the synapsed intermediate are subsequently processed by the ERCC1/XPF endonuclease, and the gaps generated are filled and sealed by uncharacterized DNA polymerase(s) and DNA ligase(s) (5, 15). Notably, SSA is generally considered mutagenic as it is associated with loss of DNA repeats. Notably, aside from the extent of DNA end resection at DSBs, activation and engagement of the mechanistically distinct DSB repair pathways can be influenced by cell cycle phase, DSB chromosomal location, and preexisting epigenetic marks at the DSB landscape (16–18).

53BP1 mediates NHEJ events and is pivotal in programmed DSBs repair, including long-range V(D)J recombination and class-switch recombination (19, 20). 53BP1 is recruited to DSB-flanking chromatin via multivalent interactions involving H2AK15ub (21), H4K20me2 (22), and the nucleosome acidic patch (23), where it has been proposed to protect DSBs from DNA end processing, thereby antagonizing HR and SSA. As such, 53BP1 and its downstream effectors RIF1 (24–28), PTIP (29), REV7/MAD2L2 (30, 31), and Shieldin/FAM35A (32, 33) act in concerted efforts to tilt the balance of DSB repair pathway choice in favor of NHEJ. Indeed, unrestrained 53BP1 activities are associated with telomeric fusions and toxic NHEJ repair products (34). Interestingly, not only does 53BP1 inactivation restore HR and contribute to resistance to PARP inhibitors in

Significance

53BP1 restrains DNA end resection, and its dosage imbalance upsets DNA double-strand break (DSB) repair pathway choice. Here, by monitoring 53BP1 distribution on DSB-flanking chromatin, we have established a dose-dependent role of the RING finger protein RNF169 in limiting 53BP1 DSB deposition. Moreover, we found that forced expression of RNF169 overcomes 53BP1 activity and stimulates mutagenic DSB repair via the single-strand annealing pathway. Our findings suggest that aberrant expression of RNF169 may represent a deleterious factor in DSB repair control and in maintenance of genome stability.

Author contributions: L.A., J.H., C.-h.Y., and M.S.Y.H. designed research; L.A., C.D., and J.L. performed research; J.C., J.Y., and J.H. contributed new reagents/analytic tools; L.A., C.D., J.L., J.C., K.M.C., C.-h.Y., and M.S.Y.H. analyzed data; and L.A. and M.S.Y.H. wrote the paper.

The authors declare no conflict of interest.

This article is a PNAS Direct Submission.

[1]To whom correspondence should be addressed. Email: huen.michael@hku.hk.

This article contains supporting information online at www.pnas.org/lookup/suppl/doi:10.1073/pnas.1804823115/-/DCSupplemental.

Published online August 13, 2018.

BRCA cancer cells (35–37), but 53BP1 nullizygocity rescues embryonic lethality of BRCA1-deficient animals (38), highlighting the interplay of 53BP1 and BRCA proteins in DSB repair control. Recent evidence also implicates a role of 53BP1 in allowing limited DSB resection to foster high-fidelity HR over mutagenic SSA repair (39). Another branch of HR-inhibiting activities is encoded by the RAP80–BRCA1 complex, which accumulates at the DSB-flanking chromatin by recognizing RNF8/RNF168-catalyzed K63-linked ubiquitin structures (40), and is antagonized by ZMYM3 (41). In reminiscence to 53BP1, RAP80 docking at DSBs correlates with inhibited DSB resection (42, 43), and RAP80 silencing results in hyperactive HR and SSA (41, 43–46).

The Ring Finger protein RNF169 is emerging as a molecular rheostat that limits 53BP1 and RAP80 deposition at the ubiquitin-modified DSB-flanking chromatin to drive high-fidelity HR repair (47–50). While elegant structural studies have unveiled the mechanistic bases that underlie the functional competition between 53BP1 and RNF169 at DSBs (23, 51, 52), exactly how this fine balance is coupled to the choice of DSB repair pathways remains to be established.

Results

RNF169 Limits 53BP1 and RAP80 Deposition at A*si*SI-Induced DSBs. RNF169 suppresses the loading of DNA damage mediator proteins 53BP1 and RAP80 at ionizing radiation-induced foci (IRIF) (47–49). The fact that a subset of RNF169-overexpressing cells still supported formation of 53BP1 IRIF (*SI Appendix*, Fig. S1*A*) suggests that RNF169 and 53BP1 may cooccupy DSB-flanking chromatin domains. Analysis of endogenous RNF169 and 53BP1 in IR-treated HeLa cells confirmed that both DNA damage response (DDR) proteins coexist at IRIF (*SI Appendix*, Fig. S1*B*). To illuminate the spatial distribution of RNF169 and 53BP1 at IRIF, we visualized IRIF in U2OS cells engineered to stably express Flag epitope-tagged RNF169 using superresolution structured illumination microscopy (SR-SIM). Anti-Flag antibodies (M2) were used in place of anti-RNF169 antibodies because the former allowed better visualization of RNF169 subcellular localization. Notably, cells that stably express Flag epitope-tagged RNF169 supported the formation of 53BP1 foci following IR treatment at frequencies similar to parental U2OS cells (>95%). Accordingly, we found that Flag-RNF169 and 53BP1 were oriented in juxtaposition to each other (*SI Appendix*, Fig. S1*C*), supporting the idea that the competing activities may occupy different chromatin domains surrounding DSBs.

To better dissect how RNF169 and 53BP1 are distributed along the DSB-flanking chromatin, we took advantage of the DIvA (DSB-induced via A*si*SI) platform, wherein DSBs can be induced at A*si*SI-target sequence across the human genome (53, 54). Pretreatment of A*si*SI-ER-U2OS cells with 4-hydroxy tamoxifen (4-OHT) triggers the nuclear translocation of the A*si*SI endonuclease and results in 100–200 site-specific DSBs (Fig. 1*A*). To study how RNF169 may serve as a molecular rheostat to modulate the deposition of 53BP1 and other DDR factors at DSBs, we also assembled a doxycycline (Dox)-inducible RNF169 expression cassette, and stably integrated it into A*si*SI-ER-U2OS cells (hereafter referred to as DIvA-eRNF169; Fig. 1*A*). We first validated that the antagonistic effects of RNF169 on 53BP1 and RAP80 accumulation at IRIFs can be recapitulated at A*si*SI-induced DSBs by indirect immunofluorescence staining experiments using in-house antibodies described previously (48, 50). Accordingly, ectopic expression of RNF169 (eRNF169) led to marked reduction of 53BP1 and RAP80 foci at A*si*SI-induced DSBs (*SI Appendix*, Fig. S2 *A* and *B*) and did not noticeably affect γH2AX foci formation (*SI Appendix*, Fig. S2*C*). RNF169 is targeted to DSBs via its ubiquitin-binding MIU2 domain where it displaces 53BP1 and RAP80 (47–49, 52). Consistent with the requirement of RNF169 MIU2 in antagonizing 53BP1 docking at DSBs, 53BP1 foci number and intensity were indistinguishable in cells expressing an RNF169 MIU2-deletion mutant (eRNF169ΔMIU2) compared with mock-treated cells (*SI Appendix*, Fig. S2*D*). To explore whether the RNF169-encoded inhibitory effect on 53BP1 deposition at A*si*SI-induced DSBs may be regulated in a cell cycle-dependent manner, we synchronized DIvA-eRNF169 cells at different cell cycle phases and quantified 53BP1 foci-positive cells following A*si*SI induction. Because ectopic expression of RNF169 efficiently suppressed 53BP1 foci in all cell populations (*SI Appendix*, Fig. S2 *E* and *F*), we concluded that RNF169 is proficient in limiting 53BP1 deposition at A*si*SI-induced DSBs in a cell cycle-independent manner.

Spatial Distribution of RNF169 and 53BP1 at A*si*SI-Induced DSBs. While RNF169 and 53BP1 competes for binding to ubiquitylated nucleosomes in vitro (51, 52) and to RNF168-modified chromatin in vivo (47–49), the opposing activities can be observed at individual IRIF (*SI Appendix*, Fig. S1 *B* and *C*), suggesting that RNF169 and 53BP1 may cooccupy DSB-flanking chromatin. To best recapitulate the dynamic equilibrium of RNF169 with 53BP1 and other DDR factors at DSBs, we titrated in reducing concentrations of doxycycline such that eRNF169 may be expressed at near endogenous levels in DIvA-eRNF169 cells. We envisage that under such circumstances eRNF169 and 53BP1 may coexist at A*si*SI-induced DSBs. Indeed, we found an inverse relationship between dose of doxycycline (eRNF169 expression) and percentage of 53BP1 foci-positive cells, in line with the competitive nature of RNF169 and 53BP1 occupancy at DSBs (*SI Appendix*, Fig. S3 *A* and *B*). Importantly, immunolabeling studies performed in DIvA-eRNF169 cells pretreated with 0.02 μg/mL doxycycline revealed coexistence of eRNF169 with γH2AX, 53BP1, and RAP80 at A*si*SI-induced DSBs (*SI Appendix*, Fig. S3 *C*–*E*). Doxycycline-treated DIvA-eRNF169 cells were subsequently processed to determine the subcellular localization of eRNF169 and its relationship with 53BP1 and RAP80 at A*si*SI-induced DNA damage foci using SR-SIM. Consistent with those observed at IRIF (*SI Appendix*, Fig. S1*C*), we found that eRNF169 and 53BP1 were often oriented in juxtaposition at A*si*SI-induced DNA damage foci (Fig. 1*B*). By contrast, eRNF169 overlapped extensively with RAP80 (Fig. 1*C*). The differential occupancy of RNF169 and 53BP1 at A*si*SI-induced DSBs was also similarly observed when DIvA-eRNF169 cells were imaged using stochastic optical reconstruction microscopy (STORM; Fig. 1*D*). Together, these results suggest that RNF169 and 53BP1 may occupy distinct chromatin territories at DSBs.

To test the possibility that RNF169 and 53BP1 may occupy distinct DSB-flanking chromatin domains, we performed chromatin immunoprecipitation (ChIP) experimentations to profile the distribution of eRNF169 and a panel of DDR factors at two previously characterized A*si*SI-induced DSBs on Chromosome 1 (i.e., Chr1_6 and Chr1_12) (53) (Fig. 1*E*). Specifically, we determined DDR protein deposition on one side of chromatin (0.1 kb to 2 Mb) flanking each of the two A*si*SI sites. We used previously validated ChIP grade anti-Flag (M2), anti-γH2AX, and anti-53BP1 antibodies (55–57) and our in-house anti-RAP80 antibodies (*SI Appendix*, Fig. S4 *A* and *B*). Accordingly, treatment of DIvA-eRNF169 cells with 4-OHT led to substantial enrichment of γH2AX, 53BP1, and RAP80 at both DSBs compared with control cells (Fig. 1*F* and *SI Appendix*, Fig. S5*A*). Enrichment of γH2AX was detectable to as far as 1 Mb away from each of the A*si*SI sites (Fig. 1*F* and *SI Appendix*, Fig. S5*A*), results which are in line with previous ChIP-sequencing (ChIP-Seq) data that documented megabase spreading of γH2AX along DSB-flanking chromatin (53). Interestingly, whereas the 53BP1 profile along the A*si*SI-induced DSB chromatin was similar to that of γH2AX (Fig. 1*F* and *SI Appendix*, Fig. S5*A*), it contrasted with that of RAP80, which preferentially accumulated at DNA end-proximal regions (Fig. 1*F* and *SI Appendix*, Fig. S5*A*).

Notably, the inhibitory effects of RNF169 on 53BP1 and RAP80 accumulation at A*si*SI-induced DSBs observed by indirect immunofluorescence staining experiments (*SI Appendix*, Fig. S2 *A* and *B*) can be recapitulated in DIvA-eRNF169 cells pretreated with a high dose of doxycycline (*SI Appendix*, Fig. S5*A*). Indeed,

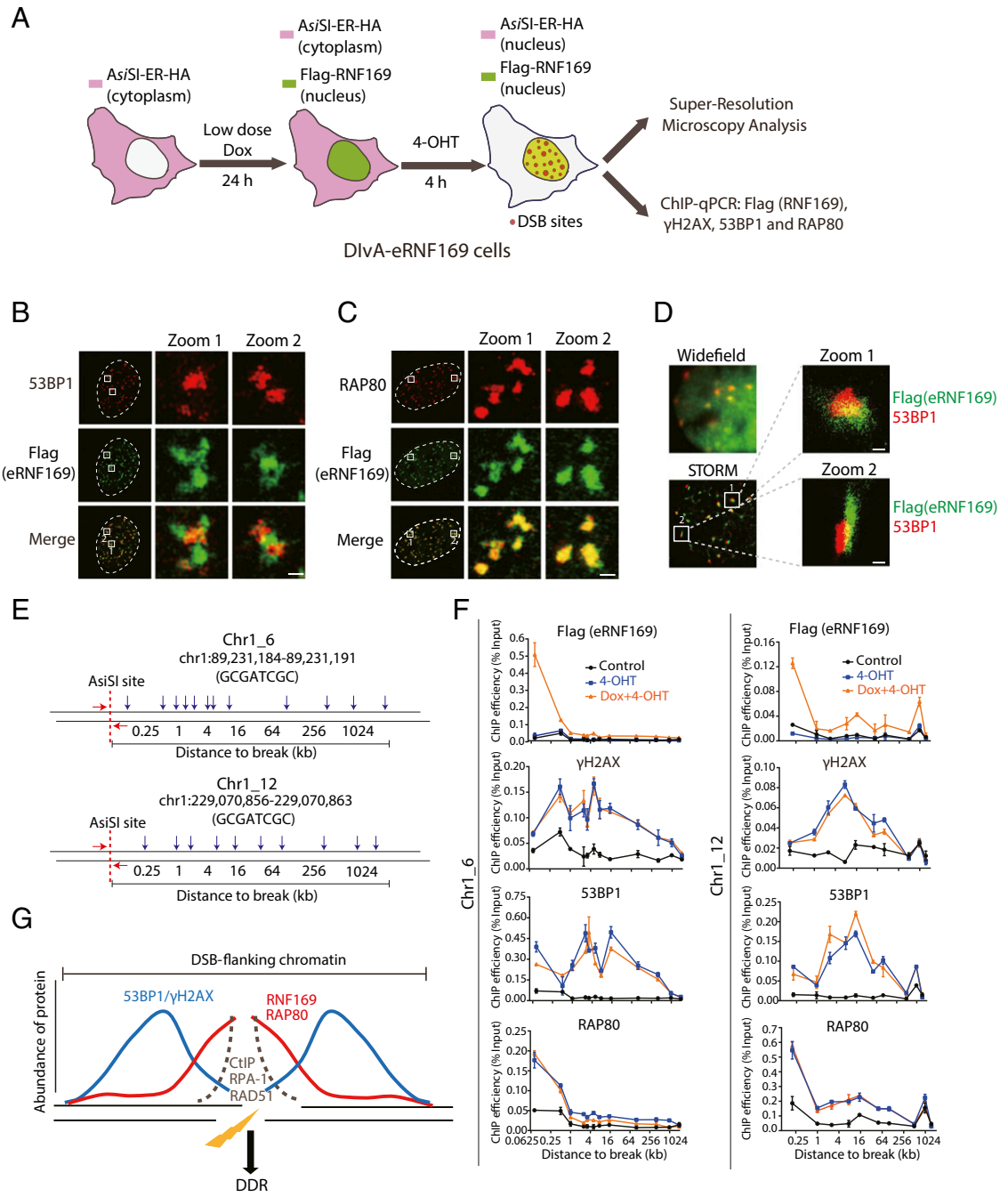

Fig. 1. Spatial distribution of RNF169 and other DDR factors at DSBs. (*A*) Schematic illustration of the DIvA platform integrated with a doxycycline (Dox)-inducible RNF169 expression cassette. (*B* and *C*) Representative SR-SIM images reveals the juxtaposed orientation of eRNF169 and 53BP1 (*B*) and colocalization of eRNF169 and RAP80 (*C*) at A*si*SI-induced DSBs. DIvA-eRNF169 cells were treated with 0.02 μg/mL doxycycline for 24 h, and 4-OHT was added 4 h before immunostaining experiments using indicated antibodies. (*D*) Representative STORM image shows the juxtaposition of eRNF169 and 53BP1 at A*si*SI-induced DSBs. (*E*) Schematic illustration of the two A*si*SI sites (Chr1_6 and Chr1_12) on Chromosome 1 used for ChIP-qPCR analysis. Each arrow represents a pair of primers employed for qPCR analysis. (*F*) ChIP-qPCR analysis of distribution of γH2AX, 53BP1, RAP80, and eRNF169 on one side of chromatin flanking each of the two A*si*SI-induced DSBs. DIvA-eRNF169 cells were treated with or without 0.02 μg/mL doxycycline for 24 h, and 4-OHT was added 4 h before cells were processed for ChIP experiments using indicated antibodies. Data represents mean ± SEM (of two technical repeats) derived from one representative experiment ($n = 3$); (*G*) Graphical illustration of DSB spatial distribution of DDR factors characterized in this study. (Scale bars: 0.5 μm.)

ChIP-qPCR analyses revealed that ectopic expression of RNF169 compromised loading of 53BP1, and to a lesser extent RAP80, onto the damaged chromatin (*SI Appendix*, Fig. S5*A*). Intriguingly, eRNF169 displayed robust accumulation at DNA end-proximal regions (*SI Appendix*, Fig. S5*A*). However, eRNF169 lacking its MIU2 did not accumulate at A*si*SI-induced DSBs and did not noticeably affect 53BP1 distribution at the DSB-flanking chromatin (*SI Appendix*, Fig. S5*B*), consistent with the requirement of RNF169 MIU2 in its targeting to DSBs (47–49). Importantly, RNF169 inactivation reproducibly led to increase of 53BP1 deposition, but not that of RAP80, at each of the two A*si*SI-induced DSBs (*SI Appendix*, Fig. S6 *A* and *B*). Together, these results validate the DIvA-eRNF169 cells as a feasible model to study the competitive relationships of RNF169 with 53BP1 at DSBs.

We next pretreated DIvA-eRNF169 cells with a low dose of doxycycline to examine how RNF169 may cooccupy with 53BP1 and RAP80 at A*si*SI-induced DSBs. At 0.02 μg/mL doxycycline, spatial distributions of γH2AX, 53BP1, and RAP80 at DSB-flanking chromatin were indistinguishable to that of control (Fig. 1*F*). Notably, we found that eRNF169 was enriched at proximal chromatin regions flanking each of the A*si*SI target sites (Fig. 1*F*), indicating that expression level change of RNF169 did not detectably affect its DSB chromatin distribution (*SI Appendix*, Fig. S5*A*). Because RNF169 promotes HR repair (47, 50), prompted by the possibility that its accumulation may reflect its functional role in driving high-fidelity DSB repair, we analyzed and compared the enrichments of CtIP, RPA-1, and RAD51 at A*si*SI-induced DSBs. Consistent with their established roles in early events in HR repair, namely DSB end resection and coating of single-strand DNA (ssDNA) overhangs, we found that CtIP, RPA-1, and RAD51 proteins were mostly deposited at DNA end-proximal chromatin regions (*SI Appendix*, Fig. S7). Together, our ChIP analyses of deposition of DDR factors at A*si*SI-induced DSBs uncovered that RNF169 and 53BP1 exhibit dissimilar distribution along the damaged chromatin domains (Fig. 1*G*) and led us to speculate that the DSB-proximal docking of RNF169 may be important in determining choice of DSB repair pathways.

Preferential Accumulation of RNF169 at HR-Prone DSBs. Because RNF169 promotes HR repair (47, 50), we next asked whether RNF169 may preferentially accumulate at HR-prone DSBs by examining RNF169 deposition at RAD51-bound DSBs (DSB IV–VI) and RAD51-unbound DSBs (DSB 1–3) as previously reported (54). We confirmed the preferential deposition of the HR factors RAD51 and RPA-1 at HR-prone DSBs, whereas γH2AX enrichment at both RAD51-bound and RAD51-unbound DSBs were similar (Fig. 2*A*). Consistent with a role in facilitating HR repair, we found that RNF169 also displayed a preference in binding to RAD51-bound over RAD51-unbound DSBs (Fig. 2*A*).

CtIP Facilitates DNA End-Proximal Accumulation of RNF169. The similar distribution patterns of RNF169 and HR factors CtIP, RPA-1, and RAD51 at A*si*SI-induced DSBs prompted us to determine the genetic regulations for RNF169 deposition at DSB-flanking chromatin (Fig. 2*B*). Although RNF169 distribution differed from that of RNF168 (*SI Appendix*, Fig. S8), RNF169 enrichment at A*si*SI-induced DSBs was hampered following small interference RNA (siRNA)-mediated inactivation of RNF168, consistent with the requirement of the classical RNF8/RNF168-mediated ubiquitination pathway in driving RNF169 IRIF formation (*SI Appendix*, Fig. S9 *A* and *B*). The observation that DSB distribution differed between RNF169 and RNF168 may reflect the maturing of the damaged chromatin, which drives the redistribution of DDR proteins along the DSB-flanking chromatin domains. Given the established roles of the MRN/CtIP complex in DSB end resection, we also

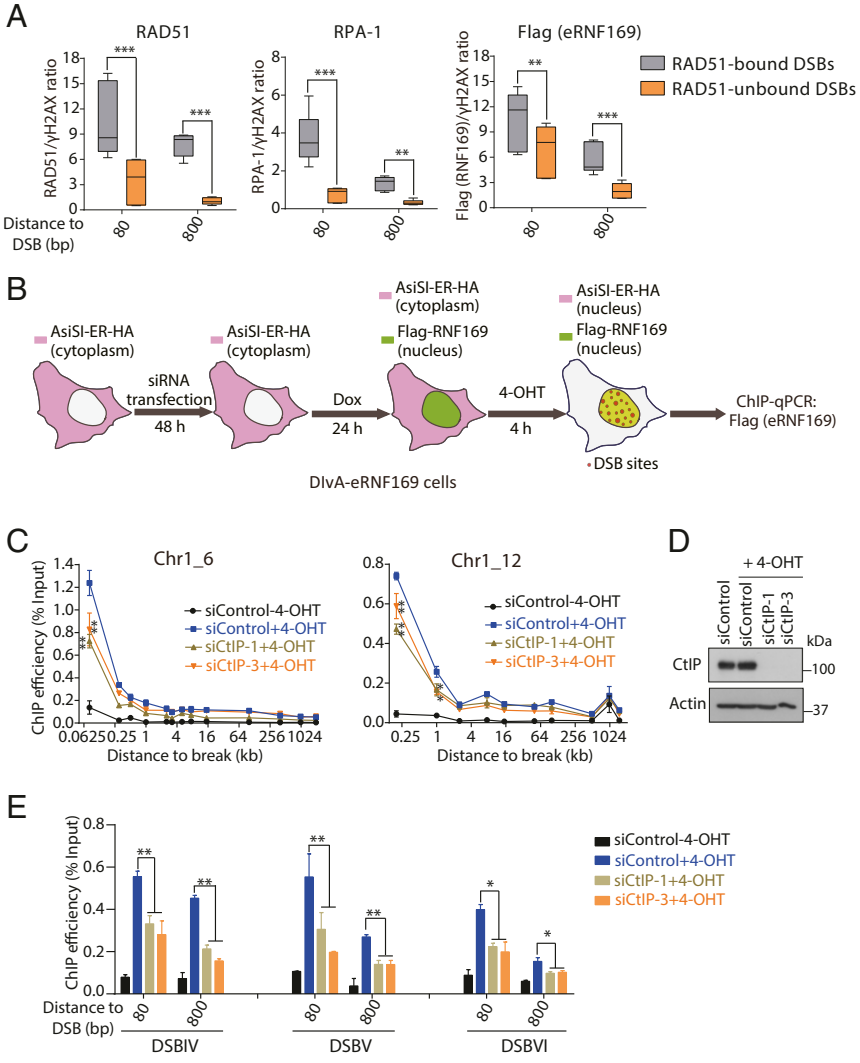

Fig. 2. Characterization of RNF169 end-proximal distribution. (*A*) RNF169 preferentially loads on RAD51-bound DSBs. DIvA-eRNF169 cells were treated as in Fig. 1*F*. ChIP-qPCR analyses were performed against γH2AX, RAD51, RPA-1, and Flag (eRNF169) at RAD51-bound and RAD51-unbound DSBs. Box and whisker plots are derived from one representative experiment (n = 3) of three technical replicates. $^{**}P < 0.01$, $^{***}P < 0.001$. (*B*) Schematic illustrating flow of experiment to define genetic requirement of DSB end-proximal accumulation of eRNF169. (*C* and *D*) CtIP promotes RNF169 accumulation at DSB end-proximal regions. DIvA-eRNF169 cells pretreated with indicated siRNAs were incubated with 1.0 μg/mL doxycycline for 24 h. 4-OHT was added to cells for 4 h. Cells were subsequently processed for ChIP experimentations using anti-Flag antibodies (eRNF169). qPCR analysis was performed to determine eRNF169 enrichments at Chr1_6 and Chr1_12. Data represents mean ± SEM (of three technical repeats) derived from one representative experiment (n = 3). $^{*}P < 0.05$, $^{**}P < 0.01$. (*D*) Western blotting experiment was performed to assess RNAi-mediated CtIP knockdown efficiency. (*E*) CtIP depletion impairs RNF169 accumulation at RAD51-bound DSBs. ChIP-qPCR experimentations and analyses were performed as in *C*.

GENETICS

tested whether the DNA end resection machineries may contribute to RNF169 accumulation at the DSB-flanking chromatin. To this end, we inactivated MRE11, NBS1, and RAD50 individually in DIvA-eRNF169 cells using the CRISPR/Cas9 method. ChIP of eRNF169 from MRN-inactivated cells did not yield quantitative change to its accumulation at A*si*SI-induced DSBs compared with control (*SI Appendix*, Fig. S9 *C* and *D*), despite robust interactions between the MRN complex and RNF169 (*SI Appendix*, Fig. S9*E*). We also silenced CtIP using two previously characterized CtIP-specific siRNAs (58, 59) and examined RNF169 loading at the two A*si*SI-induced DSBs (Fig. 2 *C* and *D*). Interestingly, we reproducibly observed a moderate reduction in RNF169 loading at proximal chromatin regions flanking each of the two DSBs (Fig. 2*C*). Moreover, accumulation of RNF169 at RAD51-bound DSBs was similarly reduced following CtIP silencing (Fig. 2*E*). On the contrary, ChIP analysis of CtIP, MRE11, and NBS1 at A*si*SI-induced DSBs were indistinguishable in control and RNF169 KO cells (*SI Appendix*, Fig. S10 *A–C*). Taken together, we propose that CtIP facilitates RNF169 accumulation on chromatin domains proximal to DSBs.

RNF169 Promotes DSB Resection. RNF169 enriched at DSB-proximal regions (Fig. 1), accumulated at RAD51-bound DSBs (Fig. 2), and promoted high-fidelity HR repair (47, 50). These observations led us to examine whether RNF169 may be involved in DSB resection. To this end, we quantitatively measured the abundance of ssDNA intermediates at A*si*SI-induced DSBs following a previously described method (60). Briefly, genomic DNA harvested from DIvA-eRNF169 cells following A*si*SI induction was pretreated with restriction enzymes (BsrGI or BanI) to digest double-strand DNAs (Fig. 3*A*). The resulting DNA preparations, including intact resected ssDNA intermediates, were subjected to qPCR quantification. We focused our analysis on two A*si*SI target sites on Chromosome 1 (DSB-α) and Chromosome 22 (DSB-β), both of which have been shown to undergo robust DNA end resection (60–62), and assayed for ssDNA intermediates at three loci that span either the BsrGI (DSB-α) or the BanI (DSB-β) restriction sites (Fig. 3*A*). We included an irrelevant site that spans a HindIII restriction site on Chromosome 22 as a negative control (No DSB; Fig. 3*A*).

Because DSB resection is activated during S/G2 cell cycle phases, to increase DSB resection efficiency and the robustness of ssDNA detection, we briefly arrested DIvA-eRNF169 cells at S/G2 cell cycle phases using thymidine before 4-OHT treatment (*SI Appendix*, Fig. S11*A*). Accordingly, A*si*SI induction resulted in a substantial increase in the abundance of ssDNA intermediates at both "DSB-α" and "DSB-β" sites, but not at the "No DSB" site (Fig. 3 *B* and *C*). ssDNA intermediates were more readily detected at DSB proximal regions, consistent with the nature of DSB resection regulation (Fig. 3 *B* and *C*). Inactivation of CtIP by siRNAs suppressed ssDNA generation, consistent with its roles in initiation of DSB resection (63) (Fig. 3 *B–D*). We further tested the effects of BRCA1 and EXO1 depletion on ssDNA generation since both DDR factors are associated with the DSB resection process (64, 65). Results showed that the ssDNA generation was moderately but significantly decreased in BRCA1-depleted or EXO1-depleted cells (Fig. 3 *B–D*). Notably, RNF169 depletion by two independent previously characterized siRNAs (48) similarly led to reduction in the abundance of ssDNA intermediates at the A*si*SI-induced DSB sites, indicating that RNF169 may facilitate DSB end resection (Fig. 3 *B–D*). To further corroborate this idea, we generated RNF169 knockout (KO) A*si*SI-ER-U2OS cells and found that level of ssDNA intermediates was also modestly reduced (*SI Appendix*, Fig. S11 *B–D*). By contrast, deficiency of both 53BP1 and RAP80 reproducibly led to increased abundance of ssDNA intermediates (*SI Appendix*, Fig. S11 *B–D*), results that are in line with their established roles in limiting DSB resection (24, 43, 45, 60). We concluded that RNF169 promotes DSB end resection.

RNF169 Promotes Homology-Mediated DSB Repair. We next assessed the roles of RNF169 in DSB repair using established cell reporters that measure DSB repair events mediated by HR, SSA, and aNHEJ and total NHEJ, respectively (66, 67). Because of the putative role of RNF169 in facilitating DSB end resection (Fig. 3 *B* and *C* and *SI Appendix*, Fig. S11 *B* and *C*), we speculated that RNF169 may be specifically required for resection-dependent DSB repair, namely, HR, SSA, and aNHEJ. Accordingly, the DSB repair reporter cells harbor a disrupted GFP gene, and expression of intact GFP requires successful repair of an I-SceI–induced DSB at the gene locus, and can be quantified by flow cytometric analysis (Fig. 3 *E–H*, *Top*) (66). We silenced RNF169 using two individual siRNAs (48), and found that RNF169 inactivation compromised high-fidelity HR repair, results that are entirely consistent with previously described (47, 50). The core HR factor PALB2 served as a positive control (Fig. 3*E*). Importantly, SSA and aNHEJ repair efficiencies were also significantly reduced following RNF169 silencing, as were that in RAD52-depleted and Polθ-depleted cells, which were used as positive controls to assess SSA and aNHEJ, respectively (Fig. 3 *F* and *G*). By contrast, we did not observe robust change in NHEJ repair efficiency in RNF169 knockdown cells (Fig. 3*H*). Together, these data suggested that RNF169 promotes (micro)homology-directed DSB repair, consistent with its role in facilitating DSB resection.

RNF169 Dose-Dependently Regulates SSA Repair. Inspired by the role of eRNF169 in limiting DSB deposition of 53BP1 and RAP80, we tested whether forced expression of RNF169 may overcome the 53BP1-imposed and RAP80-imposed barrier to resection-dependent DSB repair processes. To this end, we overexpressed RNF169 in the DSB repair reporter cells, and surprisingly, found that RNF169 specifically stimulated SSA repair (Fig. 4 *A* and *B* and *SI Appendix*, Fig. S12 *A–C*). RNF169-driven SSA repair also required its MIU2 domain (Fig. 4 *A* and *B*), suggesting that RNF169 promotes SSA by antagonizing 53BP1 and/or RAP80. Noting that 53BP1 KO cells also supported hyperactive SSA (Fig. 4 *C* and *D*) (68), we tested whether 53BP1 inactivation may reverse the stimulating effect of RNF169 on SSA. Indeed, we found that the RNF169-stimulated SSA was largely attenuated in 53BP1 KO cells (Fig. 4 *E* and *F*), indicating that RNF169 promotes SSA, at least in part, by counteracting 53BP1. We further examined whether 53BP1 deficiency may restore SSA repair to normal levels in a RNF169-deficient background. Consistent with the idea that the RNF169-53BP1 balance modulates SSA repair, we found that coinactivation of RNF169 and 53BP1 restored SSA to levels observed in otherwise wild-type control cells (Fig. 4 *G* and *H*). It is noteworthy to mention that 53BP1 deficiency did not alleviate the HR defects seen in RNF169 knockdown cells (*SI Appendix*, Fig. S13 *A* and *B*), highlighting a more specific role of 53BP1 in counteracting RNF169-dependent SSA repair.

RNF169 Stimulates SSA Repair in HR-Deficient Cells. Given that 53BP1 loss alleviates defects in DSB resection in BRCA cells (35–37), our observation that RNF169 may regulate SSA repair by counteracting 53BP1 activity led us to examine the regulation of RNF169-driven SSA in BRCA1-deficient, BRCA2-deficient, and PALB2-deficient cells. We therefore tested for a more specific role of RNF169 in modulating SSA repair in BRCA-deficient backgrounds. Accordingly, BRCA1 silencing impaired SSA (Fig. 5), consistent with its roles in multiple steps of DSB resection and DSB repair pathways (69). Inactivation of the core HR factor BRCA2 and PALB2, however, resulted in hyperactive SSA (Fig. 5), an observation that is in line with the competition between SSA and HR (70, 71). Interestingly, consistent with its dose-dependent stimulating effect on SSA repair, cells overexpressing RNF169 supported substantially elevated SSA in BRCA1-silenced, BRCA2-silenced, and PALB2-silenced cells (Fig. 5 *A* and *B*), whereas inactivation of RNF169 in BRCA2-silenced and PALB2-silenced cells, but not BRCA1-deficient cells, led to marked reduction of the otherwise hyperactivated SSA (Fig. 5 *C* and *D*). Together with the observation where forced expression of RNF169 did not affect HR repair in BRCA1, PALB2, or BRCA2 knockdown cells

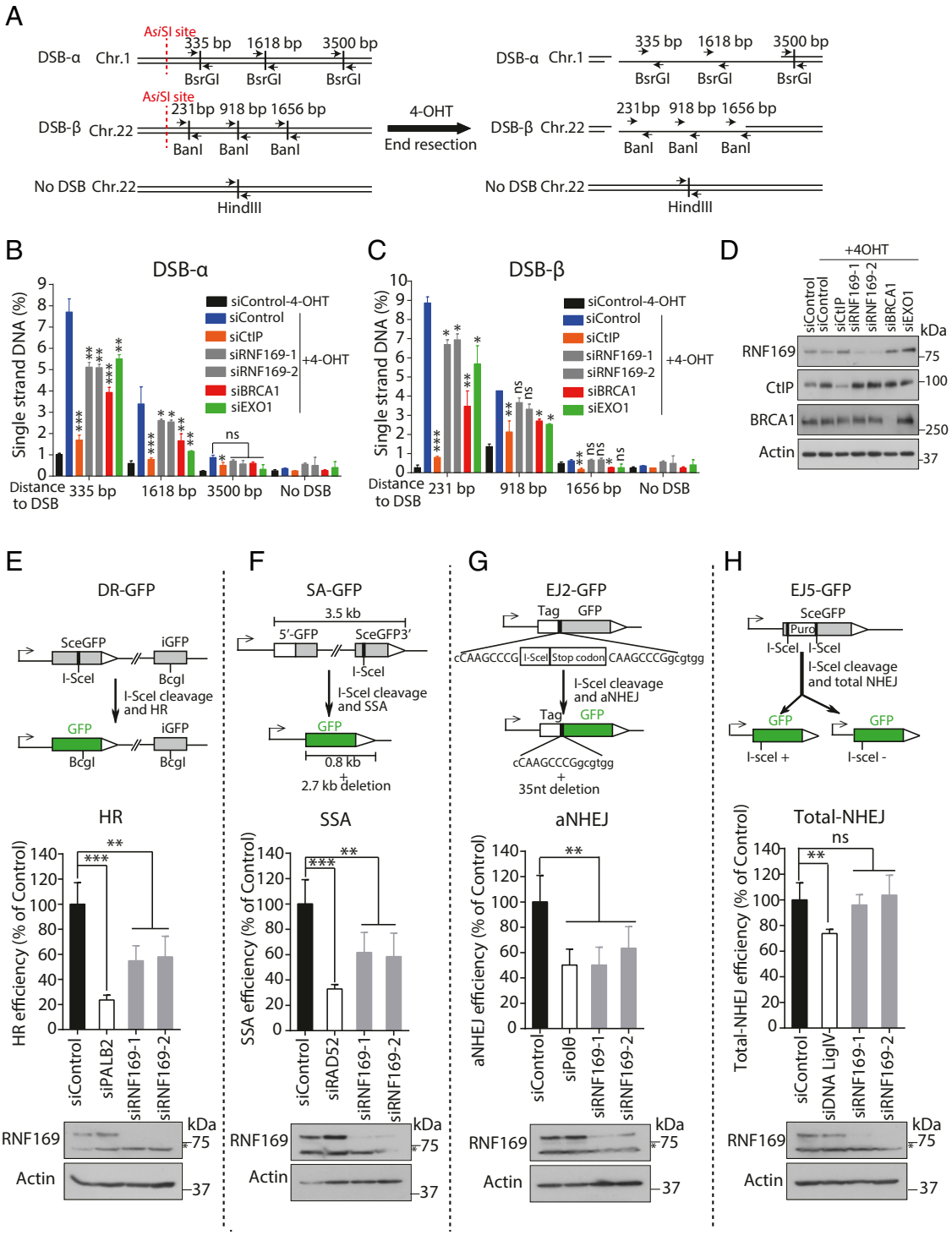

Fig. 3. RNF169 promotes DSB resection and homology-directed repairs. (*A*) Schematic for quantitative DNA resection assay based on the DIvA system. (*B* and *C*) Quantitative measurement of ssDNA generation by 5′ end resection at two A*si*SI-induced DSBs. DIvA cells pretreated with indicated siRNAs were incubated with 4-OHT for 4 h. Genomic DNA was extracted and digested with either BsrGI (*B*) or BanI (*C*). Percentage of ssDNA intermediates at indicated sites was measured by qPCR using primers indicated in *A* after restriction enzyme digestion. Data represents mean ± SEM (of two technical repeats) from three independent experiments. $*P < 0.05$, $**P < 0.01$, $***P < 0.001$; ns, not significant. (*D*) Western blotting experiment was performed to assess RNAi-mediated knockdown efficiency in cells used in *B* and *C*. (*E*–*H*) RNF169 deficiency impairs resection-dependent DSB repair. Schematic representation of the DR-GFP, SA-GFP, EJ2-GFP, and EJ5-GFP reporters to analyze the repair of I-SceI-induced DSBs by HR, SSA, aNHEJ, and total NHEJ events (*Top*). U2OS cells stably expressing DR-GFP (*E*), SA-GFP (*F*), EJ2-GFP (*G*) and EJ5-GFP (*H*) were transfected with indicated siRNAs and were electroporated with plasmid encoding the I-SceI endonuclease. (*Middle*) Flow cytometric analysis of GFP-positive cell population was performed 48 h after electroporation. Data represents mean ± SEM from three independent experiments, $**P < 0.01$, $***P < 0.001$; ns, not significant. (*Bottom*) Knockdown efficiencies were determined by Western blotting.

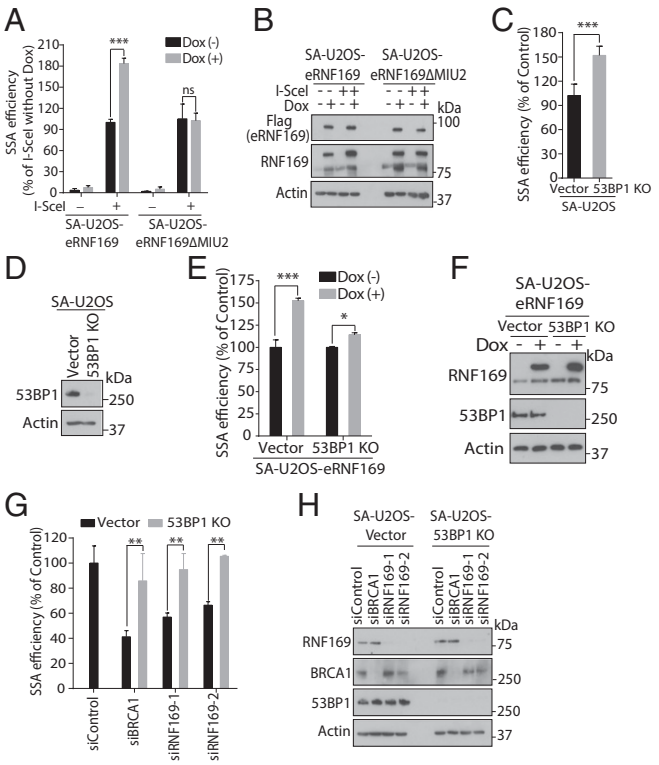

Fig. 4. RNF169 stimulates SSA repair by counteracting 53BP1. (*A*) Ectopic expression of RNF169 but not RNF169MIU2 stimulates SSA repair. SA-U2OS-eRNF169 or SA-U2OS-eRNF169ΔMIU2 cells were electroporated with plasmid encoding the I-SceI endonuclease. Cells were cultured with or without 2 μg/mL doxycycline for 48 h before cells were harvested for flow cytometric analysis. Mock electroporation (no I-SceI) was used as negative control. Data represents mean ± SEM from three independent experiments, $***P < 0.001$, ns, not significant. (*B*) Western blotting analysis showing expression of RNF169 (wild-type and ΔMIU2 mutant). (*C*) 53BP1 inactivation promotes SSA repair. SA-U2OS (vector control and 53BP1 KO) cells were electroporated with I-SceI expression construct and percentage of cells positive for GFP was analyzed 48 h after electroporation. Data represents mean ± SEM from three independent experiments, $***P < 0.001$. (*D*) Western blotting analysis to determine 53BP1 expression. (*E*) RNF169-driven SSA repair was alleviated in 53BP1 KO cells. Parental SA-U2OS-eRNF169 cells (Vector) or its 53BP1 KO derivative were treated and processed as described in *A*. Data represents mean ± SEM from three independent experiments, $*P < 0.05$, $***P < 0.001$. (*F*) Western blotting analysis to determine RNF169 expression in cells used in *E*. (*G*) 53BP1 deficiency restores SSA repair in RNF169-inactivated cells. Parental SA-U2OS cells (Vector) or its 53BP1 KO derivative were transfected with indicated siRNAs. Cells were treated and processed as described in *C*. Data represents mean ± SEM from three independent experiments, $**P < 0.01$. (*H*) Western blotting analysis was performed to assess RNAi-mediated knockdown efficiency in cells used in *G*.

(*SI Appendix*, Fig. S13 *C* and *D*), our findings suggest that RNF169 specifically fine-tunes SSA repair in BRCA cells.

Role of RAP80 in RNF169-Dependent DSB Repair. Our ChIP profiling and superresolution imaging experimentations revealed overlapping distribution of RNF169 and RAP80 at DSB-flanking chromatin domains (Fig. 1 *C* and *F*). In addition to its documented roles in restricting DSB resection (42, 43), RAP80 knockdown cells also displayed hyperactive HR and SSA repair (41, 43–45). Because eRNF169 also limited RAP80 deposition at DSBs (*SI Appendix*, Figs. S2*B* and S5*A*), we studied the antagonistic relationships between RNF169 and RAP80 in DSB repair control. We inactivated RAP80 using two independent RAP80-targeting gRNAs (72) and found that RAP80 deficiency coincided with hyperactive HR, SSA, and aNHEJ repair (*SI Appendix*, Fig. S14 *A*–*C*). Importantly, inactivation of RNF169 partially but significantly dampened HR, SSA, and aNHEJ repair in RAP80 null cells (*SI Appendix*, Fig. S14 *A*–*C*). Because both 53BP1 and RAP80 limits DSB end resection, and that forced expression of RNF169 specifically promoted SSA repair (Fig. 4*A*), we examined whether the RNF169-driven SSA may be attenuated in cells deficient in both 53BP1 and RAP80. Consistently, we found that cells inactivated for both RAP80 and 53BP1 effectively suppressed the stimulating effect of RNF169 in SSA (*SI Appendix*, Fig. S14 *D* and *E*), revealing a complex interplay between RNF169 and 53BP1/RAP80 in DSB repair control.

Discussion

The RING finger protein RNF169 counteracts the loading of DNA damage mediator proteins 53BP1 and RAP80 onto DSBs and has emerged as a negative regulator in DSB signal transduction (47–49). However, exactly how RNF169 fine-tunes 53BP1 and RAP80 activities to execute DSB repair has remained unknown. On the basis of the RNF169-encoded antagonism of 53BP1 and RAP80, our observations that dosage imbalance of RNF169 dysregulates DSB resection and choice of DSB repair pathways suggest that RNF169 may skew DSB repair pathways, at least in part, by restraining 53BP1-dependent and RAP80-dependent signal amplification. Indeed, the notion that DSB signal output, including the extent of DSB ubiquitylation, plays a determining role in choice of DSB repair in not unprecedented (73, 74). Previous work has identified OTUB2 as a negative regulator of the core ubiquitin ligase RNF8, where it suppresses RNF8 activity to promote high-fidelity HR repair (75). The importance of maintaining optimal RNF8 output was also unveiled recently with the identification of the E3/E4 ligase UBE4A, which enforces DSB signal output to promote optimal DSB resection and HR repair (76). Although it remains to be seen if RNF169

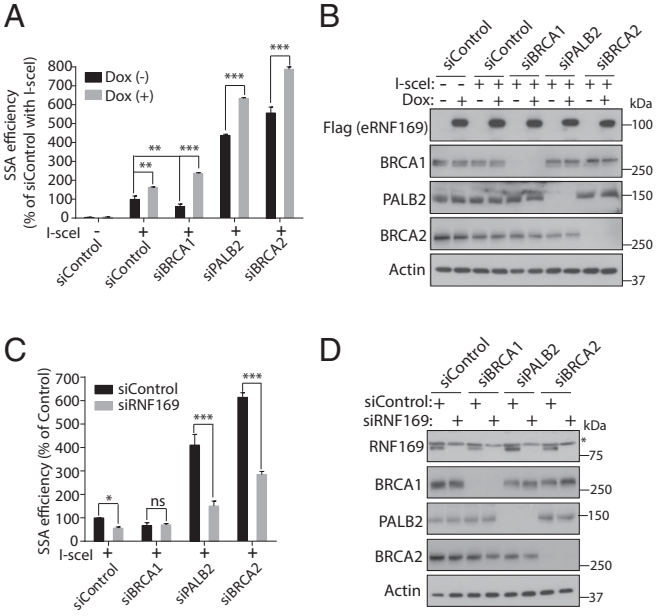

Fig. 5. RNF169 stimulates SSA repair in HR-deficient cells. (*A* and *B*) Ectopic expression of RNF169 stimulates SSA repair in BRCA1-deficient, PALB2-deficient, and BRCA2-deficient cells. SA-U2OS-eRNF169 cells pretreated with indicated siRNAs were treated and processed as described in Fig. 4*A*. Data represents mean ± SEM from four independent experiments, $**P < 0.01$, $***P < 0.001$. (*B*) Western blotting experiment was performed to assess RNAi-mediated knockdown efficiencies. (*C* and *D*) RNF169 is required for hyperactive SSA in PALB2-deficient and BRCA2-deficient cells. SA-U2OS cells were transfected with indicated siRNAs and processed as described in Fig. 4*C*. Data represents mean ± SEM from four independent experiments, $*P < 0.05$, $***P < 0.001$; ns, not significant. (*D*) Western blotting experiment was performed to assess RNAi-mediated knockdown efficiencies.

may have additional roles in DSB response control, our data adds an additional regulatory layer of DSB signal output and firmly establish the interplay of RNF169 and 53BP1/RAP80 as active regulators of DSB repair pathway choice.

Current evidence suggests that both RNF169 and 53BP1 recognize and compete for H2AK15ub-containing nucleosomes at DSBs, with RNF169 bearing higher affinity for the ubiquitin conjugate in vitro (21, 51, 52). However, exactly how the two competing activities engage in a dynamic interplay at the damaged chromatin is not clear. By recapitulating the dynamic antagonisms of RNF169 and 53BP1 at IRIFs in the DIvA platform (*SI Appendix*, Figs. S2 *A* and *B* and S5*A*), we employed super-resolution imaging to capture RNF169 and 53BP1 at A*si*SI-induced DSBs and have revealed that RNF169 is oriented juxtaposed to 53BP1 (Fig. 1 *B* and *D*), an observation supported by our ChIP experimentations (Fig. 1*F*). Interestingly, ChIP profiling of RNF169 and 53BP1 at A*si*SI-induced DSBs not only indicates that RNF169 and 53BP1 exhibit dissimilar distributions at the DSB-flanking chromatin, but also revealed that RNF169 preferentially accumulates at chromatin territories proximal to the DSBs, raising the possibility that RNF169 may contribute to the early processing of DSBs. In support of this idea, we found that RNF169 inactivation attenuated DSB end resection (Fig. 3 *B–D* and *SI Appendix*, Fig. S11 *B–D*) and led to impaired DSB repair via the HR, SSA, and aNHEJ pathways (Fig. 3 *E–G*). The fact that forced expression of RNF169-stimulated SSA repair (Figs. 4 *A* and *E* and 5*A*) but not HR or aNHEJ (*SI Appendix*, Figs. S9 *A* and *B* and S13*C*) suggests that DSB processing, especially that involving long-range DNA resection, may be more dependent on the homeostatic balance of RNF169 and 53BP1 at DSBs. This idea is supported by the observation that RNF169 silencing, much like inactivation of EXO1, did not noticeably affect CPT-induced RPA-1 foci detected by indirect immunofluorescence studies (*SI Appendix*, Fig. S15 *A–C*). Moreover, dosage imbalance of RNF169 also did not dysregulate focal accumulation nor chromatin distribution of BRCA1 and RAD51 at A*si*SI-induced DSBs (*SI Appendix*, Fig. S16 *A–C*). Considering that 53BP1 prevents hyperresection to foster high-fidelity DSB repair (39), and that 53BP1 deficiency attenuated RNF169-driven SSA (Fig. 4*E*), our findings highlight the importance of a fine balance of RNF169 and 53BP1 in proper choice of DSB repair pathways, and that RNF169 amplification may contribute to genome instability in human cancers (*SI Appendix*, Fig. S17).

Unlike the established competition between RNF169 and 53BP1 for H2AK15ub (21, 51, 52), exactly how RNF169 displaces RAP80 from DSBs is less clear. Since RNF168 promotes its own DSB recruitment by interacting with H2AK15ub (49, 51, 52), one can envisage that RNF169 may compete with RNF168 for H2AK15ub-containing nucleosomes, thereby suppressing the RNF168-dependent RAP80 recruitment onto the damaged chromatin. Alternatively, that RAP80 is targeted to DSBs via its ability to interact with both SUMO-linked and K63-linked ubiquitin polymers (77–81) raises the possibility that RNF169 may bind to additional but heretofore unidentified targets at DNA end-proximal regions surrounding DSBs, given our observations that RNF169 and RAP80 exhibit similar distribution patterns along chromatin domains that flank DSBs (Fig. 1*F*). Intriguingly, although RNF169 docks at IRIFs and A*si*SI-induced DSBs in manners that strictly require its ubiquitin-binding MIU2 domain and the primary DSB ubiquitin ligases RNF8 and RNF168 (47–49) (*SI Appendix*, Figs. S2*D*, S5*B*, and S9 *A* and *B*), we found that CtIP inactivation specifically attenuated RNF169 accrual at chromatin domains proximal to DSBs (Fig. 2 *C–E*). Considering that RNF169 interacts with the MRN complex (*SI Appendix*, Fig. S9*E*), and that RNF169 promotes DSB end resection (Fig. 3 *B–D* and *SI Appendix*, Fig. S11 *B–D*), it is tempting to speculate that the MRN/CtIP-RNF169 complex may contribute to the optimal processing of DNA ends. Although further experimentations will be required to clearly define how the MRN/CtIP-RNF169 axis contributes to optimal DNA resection, our work suggests that RNF169 shunts DSBs to resection-dependent repair, and that aberrant RNF169 expression may upset proper DSB repair pathway choice and contribute to chromosomal instability (*SI Appendix*, Fig. S18 *A–C*).

While the tumor suppressor BRCA1 may participate in multiple DSB repair pathways (69), consistent with previous reports (70, 82–84), we found that inactivation of the core HR factor PALB2 and BRCA2 led to substantially elevated SSA (Fig. 5), highlighting the complex and competitive nature of HR and SSA. Our observation is in line with the competing nature of the resection-dependent DSB repair pathways, where inactivation of HR machineries, including BRCA2 and RAD51, has been reported to fuel aNHEJ and SSA (82, 83, 85). Importantly, RNF169 promoted SSA in both PALB2 and BRCA2 proficient and deficient backgrounds (Fig. 5), highlighting an unprecedented role of RNF169 as an SSA factor. Because SSA plays an important role in mending DNA DSBs at repetitive DNA loci, noting the increased repetitive nature of higher eukaryotic genomes, it would be of significant interest to explore how RNF169 may have evolved as an RNF168 paralogue, how RNF169 supports RAD52 accumulation at DSBs (*SI Appendix*, Fig. S19), and how RNF169 expression levels correlate with stability and integrity of repetitive genomic loci. In summary, our findings uncovered the interplay of RNF169 and 53BP1 in SSA regulation, illuminate how a molecular rheostat of DSB response output contributes to DSB repair control, and implicate RNF169 as a key component in the mammalian DDR network that safeguards genome stability in higher eukaryotes (*SI Appendix*, Fig. S20).

Materials and Methods

Cell Cultures. A*si*SI-ER-U2OS cells were cultured in DMEM supplemented with 10% FBS and 1 μg/mL puromycin at 37 °C in 5% CO_2. For A*si*SI-dependent DSB induction, cells were treated with 600 nM 4-OHT (H7904; Sigma) for 4 h. The four DSB repair reporter cell lines (EJ2-U2OS, DR-U2OS, SA-U2OS, and EJ5-U2OS) were cultured in DMEM supplemented with 10% FBS and were previously described (66). For generation of cell lines with doxycycline-inducible expression of RNF169 (WT and ΔMIU2), the RNF169 cDNA was cloned in frame 3′ of the SFB (S protein, Flag, and Streptavidin-binding peptide) sequence. Cells (DIvA and the four reporter cell lines) were infected with lentiviral particles carrying RNF169 (WT and ΔMIU2)-SFB expression constructs and were subsequently selected by 2 mg/mL G418 for 1 wk. Expression of RNF169-SFB was induced by supplementing cell culture media with doxycycline (D9891; Sigma).

Generation of KO Cells by Use of the CRISPR/Cas9 Method. All KO cell lines (DIvA, DR-U2OS, and SA-U2OS) used in this study were generated using the CRISPR-Cas9 gene targeting approach. All of the guide RNAs (gRNAs) used in this study were cloned into the pLentiCRISPR v2 vectors and their sequences were as follows: MRE11 gRNA: 5′-AGTAACAATGTTGAGACCAA-3′; RAD50 gRNA: 5′-TTAAAGCCTTAGAAACACTT-3′; NBS1 gRNA: 5′-ACTGGCGTTGAGTACGTTGT-3′; RNF169 gRNA: 5′-CTGCCGCCGTCTCGTCACAG-3′; 53BP1 gRNA: 5′-CAGAATCATCCTCTAGAACC-3′; RAP80 gRNA1#: 5′-GTCGAATAGAGCAAAGTGTT-3′; RAP80 gRNA2#: 5′-GAAGAAATCACTGTTTGTCC-3′. For generation of KOs, cells were infected with lentiviral particles harboring each gRNAs twice at 24-h intervals. KO cells were allowed to grow for 1 wk before validation by Western blotting.

Lentivirus Packaging and Infection. Lentiviral particles were produced by transiently cotransfecting the lentiviral-based expression constructs together with packaging plasmids psPAX2 and pMD2.G at a ratio of 4:3:1 into HEK293T cells. Forty-eight hours after transfection, the supernatants were filtered (0.45 μm) and were applied to recipient cell lines in the presence of 8 μg/mL polybrene (Sigma).

RNA Interference. For RNAi-mediated depletion experiments, cells were transfected with two rounds of either nontargeting control or targeting siRNAs (Dharmacon) using Oligofectamine (Invitrogen). siRNAs against RNF168 were previously described (86, 87). Other target genes and their siRNA sequences are as follows: Control siRNA: 5′-UAGCGACUAAACACAUCAA-3′, RNF169 siRNA-1#: 5′-GAGCCAGACUUUAUAUUCA-3′, RNF169 siRNA-2#: 5′-GCAUCUCCGAAGAACUAAA-3′, CtIP siRNA-1#, 5′-UCCACAACAUAAUCCUAAU-3′; CtIP siRNA-2#, 5′-AAGCUAAAACAGGAACGAAUC-3′; PALB2 siRNA: 5′-GCAUAAACAUUCCGUCGAA-3′; RAD52 siRNA: 5′-GGAGUGACUCAAGAAUUAA-3′; DNA Ligase IV siRNA: 5′-AAGCCAGACAAAAGAGGUGAA-3′; Polθ siRNA: 5′-AGCUUCCACUCCUAGAAGGGA-3′; BRCA1 siRNA: 5′-GGAACCTGTCTCCACAAAG-3′;

BRCA2: 5′-GAAGAAUGCAGGUUUAAU-3′; EXO1 siRNA-1: 5-GAAGUUUCGUUACAUGUGU-3; EXO1 siRNA-2: 5- GUAAAUGGACCUACUAACA-3; EXO1 siRNA-3: 5-ACUCGGAUCUCCUAGCUUU-3; EXO1 siRNA-4: 5-GUUAGCAGCAUUUGGCAUA-3. For EXO1 depletion the four siRNAs were used as a pool.

Antibodies. Antibodies used for immunofluorescence staining, Western blotting, and ChIP are listed in *SI Appendix*, Table S1.

Immunofluorescence Staining. Cells grown on coverslips were fixed with 3% paraformaldehyde for 15 min at room temperature followed by permeabilization in 0.5% Triton solution for 30 s. A preextraction step was used when necessary and involved cell premeabilization in Triton solution for 30 s before fixation. After blocking with 3% milk at room temperature for 20 min, cells were stained by sequential incubation of primary antibodies and secondary fluorophore-conjugated antibodies (*SI Appendix*, Table S1). DAPI was used to stain nuclear DNA. Images were captured using a 60× oil immersion lens on an Olympus BX51 fluorescence microscope and were further processed by ImageJ software.

Superresolution Fluorescence Microscopy. SR-SIM imaging was performed on a Zeiss Elyra S1 microscope with 100× oil immersion lens (N.A. = 1.46). Z-stack images with 0.1 μm per step were taken between 1 and 2 μm over the glass substrate. SR-SIM images were reconstructed by ZEISS Efficient Navigation (ZEN) 2012 software, and maximum projection of the entire 1-μm volume was processed by ImageJ software. Dual-color STORM images were acquired by a SRiS (STORM) Super-Resolution Microscope (Nano BioImaging) and processed by QuickPALM in ImageJ, as previously described (88).

ChIP. ChIP was performed based on a protocol previously described with minor modifications (89). Briefly, cells were cross-linked with formaldehyde (1.42%) for 15 min at room temperature. Cross-linking was quenched by the addition of glycine (125 mM) for 5 min. Cells were washed twice with cold PBS and collected by scraping. Pelleted cells were resuspended in 300 μL of lysis buffer (50 mM Hepes/KOH, pH 7.5; 50 mM Hepes/KOH, pH 7.5; 140 mM NaCl; 1 mM EDTA; 1% Triton X-100; 0.1% Na-deoxycholate and protease inhibitors). To shear the chromatin, cells were sonicated with Bioruptor for 18 cycles (high power, 30 s on and 30 s off). After sonication, samples were diluted twice in lysis buffer and were subsequently centrifuged to clear the supernatant. Fifty microliters of supernatant were directly processed to extract total DNA as whole cell input. The remaining supernatants were transferred to new Eppendorf tubes and were incubated with indicated antibodies (*SI Appendix*, Table S1) together with prewashed protein A beads (16–157; Millipore) at 4 °C overnight. Beads were washed five times with indicated buffers and were mixed with 100 μL of 10% chelex (1421253; Bio-Rad). The samples were boiled for 10 min and centrifuged at 4 °C for 1 min. Supernatants were transferred to new tubes. After that, another 120 μL of MilliQ water was added to each beads pellet, vortex for 10 s, and were centrifuged again to spin down the beads. Combine the supernatants together as templates for follow-up qPCR analysis.

Real-Time qPCR Analysis. PCR analysis was performed on a MyiQ2 Real Time PCR Detection System (Bio-Rad) using the iTaq SYBR Green Supermix (172–5124; Bio-Rad), according to the manufacturer's instructions. All samples were analyzed in duplicates. The IP efficiency was calculated as percent of input for DNA immunoprecipitated. Primer sequences used for profiling protein distribution at Chr1_6 and Chr1_12 were listed in *SI Appendix*, Table S2. Primers used for qPCR analysis at RAD51-bound and RAD51-unbound DSBs were described (54).

Western Blotting. Cells were scraped in PBS, pelleted, and lysed in NETN buffer (20 mM Tris·HCl, pH 8.0, 100 mM NaCl, 0.5% Nonidet P-40, and 1 mM EDTA) supplemented with BitNuclease (Biotool) on ice for 15 min. Cell lysates were boiled after addition of Lamelli buffer. Proteins were separated by SDS/PAGE, transferred to PVDF membranes, which were then incubated with indicated primary and secondary antibodies (*SI Appendix*, Table S1).

In Vivo DNA End Resection Assay. Briefly, DIvA cells were treated with or without 600 nM 4-OHT for 4 h to induce A*si*SI-dependent DSBs. Thereafter, genomic DNA was purified using the standard phenol-chloroform extraction method. For each sample, around 300 ng of extracted DNA was subjected to an RNase H treatment for 15 min before mock digestion or digestion with 20 units of BsrGI (DSB-α)/BanI (DSB-β)/HindIII (No DSB) at 37 °C overnight. Samples were heat-inactivated at 65 °C for 10 min and were analyzed by qPCR. To quantify the extent of resection, around 20 ng (2 μL) of mock digested or indicated restriction enzyme digested samples were amplified by qPCR using primers listed in *SI Appendix*, Table S3. The percentage of ssDNA (ssDNA %) was calculated based on the following equation: ssDNA % = $1/(2^{Ct-1} + 0.5) \times 100$. Ct was calculated by subtracting the Ct value of the mock-digested sample from the Ct value of indicated restriction enzyme digestion sample. At least three biological repeats were performed.

Cell Cycle Analysis. To collect cells in different cell cycle phases, cells were treated with L-mimosine (M0253; Sigma) for 24 h to arrest cells in G1 phase. S and G2 phase cells were collected 7 h and 15 h upon mimosine release, respectively. To directly collect S/G2 cell populations, cells were treated with 2 mM thymidine for 18 h and further released for 4 h before harvest. Cells were trypsinized and fixed with drop-wise addition of ice-cold 70% ethanol. After overnight incubation at −20 °C, fixed cells were washed once with PBS and were treated with 200 μL of sodium citrate solution containing RNase A for 30 min at room temperature followed by addition of another 200 μL of sodium citrate solution containing 50 μg/mL propidium iodide. Cell-cycle distribution was determined using a BD FACS CantoII Analyzer.

DSB Repair Analysis in the HR, cNHEJ, SSA, and aNHEJ Reporter Cell Lines. U2OS cells stably expressing DR-GFP (DR-U2OS), EJ5-GFP (EJ5-U2OS), SSA-GFP (SSA-U2OS), and EJ2-GFP (EJ2-U2OS) (67) were transfected with indicated siRNAs and electroporated with the I-SceI expression construct (pCBASce) at 200 V, 975 microfarads using Gene Pulser XCell (Bio-Rad). Cells were further recovered for 48 h after electroporation and were subjected to for flow cytometric analysis using a BD FACS CantoII Analyzer.

Statistical Analysis. Unless otherwise stated, data represent mean ± SEM of at least three independent experiments. Student's *t* test (two-tailed) was used to evaluate statistical significance, and a $P < 0.05$ value was considered as significant.

ACKNOWLEDGMENTS. We thank Drs. Gaëlle Legube and Jeremy Stark for generous sharing of reagents and comments on the manuscript, Drs. Sandy Chang and Rekha Rai for discussion, and we acknowledge the technical advice and support from Dr. Jing Guo, and Faculty Core Facility (The University of Hong Kong) with imaging analyses. This work is supported by Research Grants Council Hong Kong Projects 17108314 and C7007-17GF (to M.S.Y.H.).

1. Bunting SF, Nussenzweig A (2013) End-joining, translocations and cancer. *Nat Rev Cancer* 13:443–454.
2. Mani RS, Chinnaiyan AM (2010) Triggers for genomic rearrangements: Insights into genomic, cellular and environmental influences. *Nat Rev Genet* 11:819–829.
3. Moynahan ME, Jasin M (2010) Mitotic homologous recombination maintains genomic stability and suppresses tumorigenesis. *Nat Rev Mol Cell Biol* 11:196–207.
4. Jackson SP, Bartek J (2009) The DNA-damage response in human biology and disease. *Nature* 461:1071–1078.
5. Verma P, Greenberg RA (2016) Noncanonical views of homology-directed DNA repair. *Genes Dev* 30:1138–1154.
6. Ceccaldi R, Rondinelli B, D'Andrea AD (2016) Repair pathway choices and consequences at the double-strand break. *Trends Cell Biol* 26:52–64.
7. Lieber MR (2008) The mechanism of human nonhomologous DNA end joining. *J Biol Chem* 283:1–5.
8. Chang HHY, Pannunzio NR, Adachi N, Lieber MR (2017) Non-homologous DNA end joining and alternative pathways to double-strand break repair. *Nat Rev Mol Cell Biol* 18:495–506.
9. Huertas P (2010) DNA resection in eukaryotes: Deciding how to fix the break. *Nat Struct Mol Biol* 17:11–16.
10. Symington LS (2016) Mechanism and regulation of DNA end resection in eukaryotes. *Crit Rev Biochem Mol Biol* 51:195–212.
11. Ivanov EL, Sugawara N, Fishman-Lobell J, Haber JE (1996) Genetic requirements for the single-strand annealing pathway of double-strand break repair in Saccharomyces cerevisiae. *Genetics* 142:693–704.
12. Do AT, Brooks JT, Le Neveu MK, LaRocque JR (2014) Double-strand break repair assays determine pathway choice and structure of gene conversion events in Drosophila melanogaster. *G3 (Bethesda)* 4:425–432.
13. Pontier DB, Tijsterman M (2009) A robust network of double-strand break repair pathways governs genome integrity during C. elegans development. *Curr Biol* 19:1384–1388.
14. Symington LS (2002) Role of RAD52 epistasis group genes in homologous recombination and double-strand break repair. *Microbiol Mol Biol Rev* 66:630–670.
15. Bhargava R, Onyango DO, Stark JM (2016) Regulation of single-strand annealing and its role in genome maintenance. *Trends Genet* 32:566–575.
16. Hustedt N, Durocher D (2016) The control of DNA repair by the cell cycle. *Nat Cell Biol* 19:1–9.
17. Lemaître C, et al. (2014) Nuclear position dictates DNA repair pathway choice. *Genes Dev* 28:2450–2463.

18. Clouaire T, Legube G (2015) DNA double strand break repair pathway choice: A chromatin based decision? *Nucleus* 6:107–113.
19. Daniel JA, Nussenzweig A (2013) The AID-induced DNA damage response in chromatin. *Mol Cell* 50:309–321.
20. Panier S, Boulton SJ (2014) Double-strand break repair: 53BP1 comes into focus. *Nat Rev Mol Cell Biol* 15:7–18.
21. Fradet-Turcotte A, et al. (2013) 53BP1 is a reader of the DNA-damage-induced H2A Lys 15 ubiquitin mark. *Nature* 499:50–54.
22. Botuyan MV, et al. (2006) Structural basis for the methylation state-specific recognition of histone H4-K20 by 53BP1 and Crb2 in DNA repair. *Cell* 127: 1361–1373.
23. Wilson MD, et al. (2016) The structural basis of modified nucleosome recognition by 53BP1. *Nature* 536:100–103.
24. Escribano-Díaz C, et al. (2013) A cell cycle-dependent regulatory circuit composed of 53BP1-RIF1 and BRCA1-CtIP controls DNA repair pathway choice. *Mol Cell* 49: 872–883.
25. Chapman JR, et al. (2013) RIF1 is essential for 53BP1-dependent nonhomologous end joining and suppression of DNA double-strand break resection. *Mol Cell* 49: 858–871.
26. Di Virgilio M, et al. (2013) Rif1 prevents resection of DNA breaks and promotes immunoglobulin class switching. *Science* 339:711–715.
27. Feng L, Fong K-W, Wang J, Wang W, Chen J (2013) RIF1 counteracts BRCA1-mediated end resection during DNA repair. *J Biol Chem* 288:11135–11143.
28. Zimmermann M, Lottersberger F, Buonomo SB, Sfeir A, de Lange T (2013) 53BP1 regulates DSB repair using Rif1 to control 5′ end resection. *Science* 339:700–704.
29. Callen E, et al. (2013) 53BP1 mediates productive and mutagenic DNA repair through distinct phosphoprotein interactions. *Cell* 153:1266–1280.
30. Xu G, et al. (2015) REV7 counteracts DNA double-strand break resection and affects PARP inhibition. *Nature* 521:541–544.
31. Boersma V, et al. (2015) MAD2L2 controls DNA repair at telomeres and DNA breaks by inhibiting 5′ end resection. *Nature* 521:537–540.
32. Gupta R, et al. (2018) DNA repair network analysis reveals shieldin as a key regulator of NHEJ and PARP inhibitor sensitivity. *Cell* 173:972–988.e23.
33. Tomida J, et al. (2018) FAM35A associates with REV7 and modulates DNA damage responses of normal and BRCA1-defective cells. *EMBO J,* 37:e99543.
34. Orthwein A, et al. (2014) Mitosis inhibits DNA double-strand break repair to guard against telomere fusions. *Science* 344:189–193.
35. Bouwman P, et al. (2010) 53BP1 loss rescues BRCA1 deficiency and is associated with triple-negative and BRCA-mutated breast cancers. *Nat Struct Mol Biol* 17:688–695.
36. Li M, et al. (2016) 53BP1 ablation rescues genomic instability in mice expressing 'RING-less' BRCA1. *EMBO Rep* 17:1532–1541.
37. Bunting SF, et al. (2010) 53BP1 inhibits homologous recombination in Brca1-deficient cells by blocking resection of DNA breaks. *Cell* 141:243–254.
38. Cao L, et al. (2009) A selective requirement for 53BP1 in the biological response to genomic instability induced by Brca1 deficiency. *Mol Cell* 35:534–541.
39. Ochs F, et al. (2016) 53BP1 fosters fidelity of homology-directed DNA repair. *Nat Struct Mol Biol* 23:714–721.
40. Huen MS, Chen J (2010) Assembly of checkpoint and repair machineries at DNA damage sites. *Trends Biochem Sci* 35:101–108.
41. Leung JW, et al. (2017) ZMYM3 regulates BRCA1 localization at damaged chromatin to promote DNA repair. *Genes Dev* 31:260–274.
42. Kakarougkas A, et al. (2013) Co-operation of BRCA1 and POH1 relieves the barriers posed by 53BP1 and RAP80 to resection. *Nucleic Acids Res* 41:10298–10311.
43. Coleman KA, Greenberg RA (2011) The BRCA1-RAP80 complex regulates DNA repair mechanism utilization by restricting end resection. *J Biol Chem* 286: 13669–13680.
44. Typas D, et al. (2015) The de-ubiquitylating enzymes USP26 and USP37 regulate homologous recombination by counteracting RAP80. *Nucleic Acids Res* 43:6919–6933, and erratum (2016) 44:2976.
45. Hu Y, et al. (2011) RAP80-directed tuning of BRCA1 homologous recombination function at ionizing radiation-induced nuclear foci. *Genes Dev* 25:685–700.
46. Park IS, et al. (2016) SUMOylation regulates nuclear localization and stability of TRAIP/RNF206. *Biochem Biophys Res Commun* 470:881–887.
47. Poulsen M, Lukas C, Lukas J, Bekker-Jensen S, Mailand N (2012) Human RNF169 is a negative regulator of the ubiquitin-dependent response to DNA double-strand breaks. *J Cell Biol* 197:189–199.
48. Chen J, Feng W, Jiang J, Deng Y, Huen MS (2012) Ring finger protein RNF169 antagonizes the ubiquitin-dependent signaling cascade at sites of DNA damage. *J Biol Chem* 287:27715–27722.
49. Panier S, et al. (2012) Tandem protein interaction modules organize the ubiquitin-dependent response to DNA double-strand breaks. *Mol Cell* 47:383–395.
50. An L, et al. (2017) Dual-utility NLS drives RNF169-dependent DNA damage responses. *Proc Natl Acad Sci USA* 114:E2872–E2881.
51. Hu Q, Botuyan MV, Cui G, Zhao D, Mer G (2017) Mechanisms of ubiquitin-nucleosome recognition and regulation of 53BP1 chromatin recruitment by RNF168/169 and RAD18. *Mol Cell* 66:473–487.e9.
52. Kitevski-LeBlanc J, et al. (2017) The RNF168 paralog RNF169 defines a new class of ubiquitylated histone reader involved in the response to DNA damage. *eLife* 6: e23872.
53. Iacovoni JS, et al. (2010) High-resolution profiling of gammaH2AX around DNA double strand breaks in the mammalian genome. *EMBO J* 29:1446–1457.
54. Aymard F, et al. (2014) Transcriptionally active chromatin recruits homologous recombination at DNA double-strand breaks. *Nat Struct Mol Biol* 21:366–374.
55. d'Adda di Fagagna F, et al. (2003) A DNA damage checkpoint response in telomere-initiated senescence. *Nature* 426:194–198.
56. Moon SH, et al. (2010) Wild-type p53-induced phosphatase 1 dephosphorylates histone variant gamma-H2AX and suppresses DNA double strand break repair. *J Biol Chem* 285:12935–12947.
57. Tang J, et al. (2013) Acetylation limits 53BP1 association with damaged chromatin to promote homologous recombination. *Nat Struct Mol Biol* 20:317–325.
58. Makharashvili N, et al. (2014) Catalytic and noncatalytic roles of the CtIP endonuclease in double-strand break end resection. *Mol Cell* 54:1022–1033.
59. Kousholt AN, et al. (2012) CtIP-dependent DNA resection is required for DNA damage checkpoint maintenance but not initiation. *J Cell Biol* 197:869–876.
60. Zhou Y, Caron P, Legube G, Paull TT (2014) Quantitation of DNA double-strand break resection intermediates in human cells. *Nucleic Acids Res* 42:e19.
61. Pfister SX, et al. (2014) SETD2-dependent histone H3K36 trimethylation is required for homologous recombination repair and genome stability. *Cell Rep* 7:2006–2018.
62. Cohen S, et al. (2018) Senataxin resolves RNA:DNA hybrids forming at DNA double-strand breaks to prevent translocations. *Nat Commun* 9:533.
63. Sartori AA, et al. (2007) Human CtIP promotes DNA end resection. *Nature* 450: 509–514.
64. Nimonkar AV, et al. (2011) BLM-DNA2-RPA-MRN and EXO1-BLM-RPA-MRN constitute two DNA end resection machineries for human DNA break repair. *Genes Dev* 25: 350–362.
65. Cruz-García A, López-Saavedra A, Huertas P (2014) BRCA1 accelerates CtIP-mediated DNA-end resection. *Cell Rep* 9:451–459.
66. Bennardo N, Cheng A, Huang N, Stark JM (2008) Alternative-NHEJ is a mechanistically distinct pathway of mammalian chromosome break repair. *PLoS Genet* 4: e1000110.
67. Gunn A, Stark JM (2012) I-SceI-based assays to examine distinct repair outcomes of mammalian chromosomal double strand breaks. *Methods Mol Biol* 920:379–391.
68. Muñoz MC, et al. (2012) RING finger nuclear factor RNF168 is important for defects in homologous recombination caused by loss of the breast cancer susceptibility factor BRCA1. *J Biol Chem* 287:40618–40628.
69. Chen C-C, Feng W, Lim PX, Kass EM, Jasin M (2018) Homology-directed repair and the role of BRCA1, BRCA2, and related proteins in genome integrity and cancer. *Annu Rev Cancer Biol* 2:1–24.
70. Anantha RW, et al. (2017) Functional and mutational landscapes of BRCA1 for homology-directed repair and therapy resistance. *eLife* 6:e21350.
71. Muñoz MC, Yanez DA, Stark JM (2014) An RNF168 fragment defective for focal accumulation at DNA damage is proficient for inhibition of homologous recombination in BRCA1 deficient cells. *Nucleic Acids Res* 42:7720–7733.
72. Ng HM, Wei L, Lan L, Huen MS (2016) The Lys63-deubiquitylating enzyme BRCC36 limits DNA break processing and repair. *J Biol Chem* 291:16197–16207.
73. Schwertman P, Bekker-Jensen S, Mailand N (2016) Regulation of DNA double-strand break repair by ubiquitin and ubiquitin-like modifiers. *Nat Rev Mol Cell Biol* 17: 379–394.
74. Kee Y, Huang TT (2015) Role of deubiquitinating enzymes in DNA repair. *Mol Cell Biol* 36:524–544.
75. Kato K, et al. (2014) Fine-tuning of DNA damage-dependent ubiquitination by OTUB2 supports the DNA repair pathway choice. *Mol Cell* 53:617–630.
76. Baranes-Bachar K, et al. (2018) The ubiquitin E3/E4 ligase UBE4A adjusts protein ubiquitylation and accumulation at sites of DNA damage, facilitating double-strand break repair. *Mol Cell* 69:866–878.e7.
77. Guzzo CM, et al. (2012) RNF4-dependent hybrid SUMO-ubiquitin chains are signals for RAP80 and thereby mediate the recruitment of BRCA1 to sites of DNA damage. *Sci Signal* 5:ra88.
78. Hu X, Paul A, Wang B (2012) Rap80 protein recruitment to DNA double-strand breaks requires binding to both small ubiquitin-like modifier (SUMO) and ubiquitin conjugates. *J Biol Chem* 287:25510–25519.
79. Kim H, Chen J, Yu X (2007) Ubiquitin-binding protein RAP80 mediates BRCA1-dependent DNA damage response. *Science* 316:1202–1205.
80. Sobhian B, et al. (2007) RAP80 targets BRCA1 to specific ubiquitin structures at DNA damage sites. *Science* 316:1198–1202.
81. Wang B, et al. (2007) Abraxas and RAP80 form a BRCA1 protein complex required for the DNA damage response. *Science* 316:1194–1198.
82. Tutt A, et al. (2001) Mutation in Brca2 stimulates error-prone homology-directed repair of DNA double-strand breaks occurring between repeated sequences. *EMBO J* 20:4704–4716.
83. Stark JM, Pierce AJ, Oh J, Pastink A, Jasin M (2004) Genetic steps of mammalian homologous repair with distinct mutagenic consequences. *Mol Cell Biol* 24: 9305–9316.
84. Obermeier K, et al. (2016) Heterozygous PALB2 c.1592delT mutation channels DNA double-strand break repair into error-prone pathways in breast cancer patients. *Oncogene* 35:3796–3806.
85. Ahrabi S, et al. (2016) A role for human homologous recombination factors in suppressing microhomology-mediated end joining. *Nucleic Acids Res* 44: 5743–5757.
86. Huen MS, et al. (2007) RNF8 transduces the DNA-damage signal via histone ubiquitylation and checkpoint protein assembly. *Cell* 131:901–914.
87. Sy SM-H, et al. (2011) Critical roles of ring finger protein RNF8 in replication stress responses. *J Biol Chem* 286:22355–22361.
88. Vancevska A, Douglass KM, Pfeiffer V, Manley S, Lingner J (2017) The telomeric DNA damage response occurs in the absence of chromatin decompaction. *Genes Dev* 31: 567–577.
89. Nelson JD, Denisenko O, Bomsztyk K (2006) Protocol for the fast chromatin immunoprecipitation (ChIP) method. *Nat Protoc* 1:179–185.